EXPERIMENTAL INVESTIGATION OF SPATIAL-MODE-SELECTIVE

FREQUENCY UP-CONVERSION

by

MOHAN GIRIBABU

Presented to the Faculty of the Graduate School of

The University of Texas at Arlington in Partial Fulfillment

of the Requirements

for the Degree of

MASTER OF SCIENCE IN ELECTRICAL ENGINEERING

THE UNIVERSITY OF TEXAS AT ARLINGTON

December 2015

Acknowledgements

Abstract

EXPERIMENTAL INVESTIGATION OF SPATIAL-MODE-SELECTIVE

FREQUENCY UP-CONVERSION

Mohan Giribabu, M.S.

The University of Texas at Arlington, 2015

Supervising Professor: Michael Vasilyev

We experimentally investigate the spatial-mode-selective frequency up-conversion by sum-frequency generation in a second-order $\chi^{(2)}$ medium. In particular, we are interested in zero and first order Gaussian modes.

In our experiment, we generate pump and signal pulses of 400 ps duration, spatially modulate them, and couple them into a Periodically Poled Lithium Niobate (PPLN) waveguide. Only one signal mode selected by the pump's spatial profile is up-converted. The up-converted signal is separated from the original signal and pump beams, modes are captured on a camera and efficiency of up-conversion is recorded. We also discuss some important phase-matching conditions for nonlinear interaction in $\chi^{(3)}$ medium.

This experiment results will help build spatial-mode de-multiplexers for both classical and quantum communication.

Table of Contents

List of Illustrations

List of Tables

Chapter 1

Introduction

Optical communication technology has been making progress very rapidly for several decades, meeting needs of our information-driven society and economy, which are increasing continuously. Much of this progress has been achieved because of finding innovative ways to increase data carrying capacity of a single optical fiber.

After significant growth over several decades, the capacity of single-mode fibers (SMFs) is approaching the capacity limits imposed by the combination of the Shannon's information theory and nonlinear fiber effects [1]. In order to meet the needs of society and to keep up with the demands in the traffic growth, a new dimension is now required and it has recently been suggested [2, 3] that space-division multiplexing (SDM) can be used as a technique to increase the capacity growth in the optical transmission system in multi-mode fiber (MMF). Multi-mode fibers can support hundreds of modes and accordingly data capacity will be increased. Considering the nonlinear effects and mode couplings, it is extremely difficult to process data at receiving end. A few-mode fiber (FMF), which supports only a few modes is an attractive alternative to MMF. In MMF and FMF, owing to the emergence of spatial-division multiplexing and also mode-division multiplexing communication systems, parametric amplification and frequency

conversion of spatially-multimode light have been recently gaining attention in both classical and quantum signal processing context. Multimode parametric amplifiers have been extensively discussed in [4-6] and those capable of noiseless phase sensitive amplification discussed in [7-9] could be an attractive solution for inline amplification in these systems, whereas "1550-nm-to-visible" frequency up-converters can be used to identify various spatial modes and to enhance single-photon detection efficiency.

An efficient way to de-multiplex orthogonal spatially-overlapping spatial modes is the field of very active current research. In addition, each resolved spatial mode needs to be efficiently detected. Single-photon detection or high-efficiency detection of faint infrared light is very important for many applications such as in military, communication, biomedical imaging, and quantum optics. The dark counts of infrared avalanche photodetectors (APDs) based on InGaAs are much higher than those of silicon detectors operating in visible range. Implementation of the BB84 key distribution protocol [10] using a 1550 nm source found the optimal efficiency of the InGaAs detector of 11% [11], while detector efficiency of 20% at best is achievable [12–13] for the infrared InGaAs detectors. The noisy infrared detection can be avoided by converting photons from infrared to visible by means of frequency up-conversion [14]. Especially for quantum information application, where avoidance of noise is critical, infrared-to-visible frequency conversion is the best way to avoid noise.

Frequency up-conversion is a nonlinear optical process based on sum-frequency generation (SFG). The two input optical signals combine in a nonlinear medium to generate a third signal at a frequency equal to the sum of the two inputs. A 100% conversion efficiency can be realized in the nonlinear media with large nonlinearity and / or by employing a strong pump field. Detection of visible photons replicates that of infrared photons, and thus with the help of this nonlinear effect in nonlinear crystals, silicon APDs could replace InGaAs/InP APDs in infrared photon detection. This is one of the applications of frequency up-conversion.

Recently, 70% conversion efficiency and low-noise frequency up-conversion has been demonstrated by sum-frequency mixing in a periodically poled $LiNbO_3$ (PPLN) waveguide [15], in which 1302 nm photons were up-converted to 709 nm photons by using 1556 nm pump. As high as 50% external efficiency was seen obtained with continuous-wave (CW) pumping. By incorporating spatial filtering much better efficiency and low noise could be achieved. Similar work is demonstrated in [16], where efficient single-photon detection at 1550 nm is done by means of sum-frequency mixing with a strong pump at 1064 nm in PPLN waveguide, followed by photon counting in visible region. Up-frequency conversion efficiency of 90% was seen at 21.6 W of circulation power in resonant pump cavity with a 400 mW laser. A simple approach for tunable up-conversion was proposed [17] for both single-photon detection or for low-light-level

detection. A tenfold increase in detection bandwidth was reported using the scheme where a tunable pump laser source is used for frequency up-conversion in a periodically poled lithium niobate (PPLN) and a low-jitter silicon avalanche photodiode is used.

The unitary nature of SFG process permits the preservation of the signal quantum state in the process of frequency up-conversion. This has lead to the proposal of an experimental scheme [18], in which the quantum states of two light beams of different frequency can be interchanged. The same unitary nature also helped in the first experimental realization [19] of quantum frequency conversion, where an input light beam of one frequency was converted to output light beam of another frequency while preserving the quantum state. Theoretical work on frequency up-conversion of an arbitrary spatially-broadband quantum state (quantum image) was done in [20]. This work shows that quantum image up-conversion could be obtained in PPLN crystals with 99% efficiency at moderate up-conversion pump intensities that are well below the PPLN damage threshold. This work also indicates the practicality of the quantum image up-conversion with readily available solid-state or fiber-based pump sources.

Multimode waveguides are the best solution to achieve the high conversion efficiency at practical levels of pump power. The spatial mode coupling during second-harmonic generation was discussed in [21, 22]. Odd and even modes were coupled into waveguide for sum-frequency generation by using integrated mode

4

converters and advanced quasi-phase-matching techniques [23, 24]. Recently, the mode coupling in the spontaneous parametric down-conversion process were observed in vertically-multimode periodically-polled potassium titanyl phosphate (PPKPT) waveguide [25, 26].

This thesis starts with the theoretical study of nonlinear optical phenomena in $\chi^{(3)}$ material, few-mode fiber (FMF), which supports four modes. Phase-matching condition for four-wave mixing in two-mode case is derived and discussed in chapter 2. Also, we present the computed values of the effective areas of interaction for self-phase modulation (SPM), cross-phase modulation (XPM), and four-wave mixing (FWM).

In the rest of the thesis, experimental demonstration of spatially-mode-selective frequency up-conversion is reported in a two-mode periodically-polled lithium niobate (PPLN) waveguide for signal of wavelength 1540 nm and moderate pump power. Experimental setup of pulse generation, modulation, coupling, and detection is described in detail in chapter 3. Results on frequency up-conversion efficiency and spatial-mode selectivity are reported in chapter 4.

Chapter 5 summarizes the thesis, and chapter 7 (Appendices) lists the parts used in the experimental setup and the temperature controller for PPLN waveguide.

Chapter 2

Background

2.1 Second-order nonlinear interactions in a waveguide

In the following chapter, theoretical information on sum-frequency generation (SFG) is presented. When an intense laser field is incident on a material, nonlinear response of the material can cause polarization of the medium to generate new frequency components which were not present in the incident field. The nonlinear response of the medium can be expressed in terms of polarization $\vec{P}(t)$ as a power series in the electric field strength $\vec{E}(t)$,

$$\vec{P}(t) = \varepsilon_0 \left[\chi^{(1)} \vec{E}(t) + \chi^{(2)} \vec{E}^2(t) + \chi^{(3)} \vec{E}^3(t) + \dots \right], \qquad (2.1.1)$$

$$\vec{P}(t) = \vec{P}^{(1)}(t) + \vec{P}^{(2)}(t) + \vec{P}^{(3)}(t) + \dots , \qquad (2.1.2)$$

where ε_0 is the permittivity of free space, $\chi^{(1)}$ is the linear susceptibility, and $\chi^{(2)}$ and $\chi^{(3)}$ are second-order and third-order nonlinear optical susceptibilities, respectively. In Equation (2.1.2) polarization of the medium is expressed in terms of linear and nonlinear polarizations. $\vec{P}^{(2)}(t) = \varepsilon_0 \chi^{(2)} \vec{E}^2(t)$ is the second-order nonlinear polarization and $\vec{P}^{(3)}(t) = \varepsilon_0 \chi^{(3)} \vec{E}^3(t)$ is the third-order nonlinear polarization. The physical processes that occur because of second-order nonlinear polarization and because of the third-order nonlinear polarization tend to differ. Third-order nonlinear polarization can be seen in all materials (centrosymmetric

6

and noncentrosymmetric), whereas second-order nonlinear polarization effects exist only in the non-centrosymmetric crystals. In non-centrosymmetric crystals both second-order and third-order polarization occur, but third-order effects are too weak to observe.

Sum-frequency generation (SFG) is one such nonlinear optic process that occurs because of the second-order nonlinear polarization. In SFG, two distinct frequency components of which one is signal at frequency ω_s and the other is pump at ω_p interact nonlinearly to produce sum frequency wave at $\omega_{sfg} = \omega_s + \omega_p$. The wave equation, valid for all frequency components in a nonlinear medium is defined by

$$\nabla^2 \vec{E}_n - \frac{\varepsilon^{(1)}(\omega_n)}{c^2} \frac{\partial^2 \vec{E}_n}{\partial t^2} = \frac{1}{\varepsilon_0 c^2} \frac{\partial^2 \vec{P}_n^{\text{NL}}}{\partial t^2} \quad , \tag{2.1.3}$$

where index $n = s$, p or "sfg", $\vec{P}_n^{\text{NL}}$ is the nonlinear polarization, c is speed of light in free space, ε_0 is the free-space permittivity and $\varepsilon^{(1)}$ is the relative permittivity. In the absence of nonlinear polarization, the solution to (2.1.3) at ω_{sfg} propagating in $+z$ is

$$E_{sfg} = A_{sfg}(0)e^{i(k_{sfg}z - \omega_{sfg}t)} + c.c. , \tag{2.1.4}$$

where A_{sfg} is the amplitude and it is constant, and $k_{sfg} = \dfrac{n_{sfg}\omega_{sfg}}{c}, n_{sfg}^2 = \varepsilon^{(1)}(\omega_{sfg})$ is the wave vector. If we consider the nonlinear source term, the solution above still

holds true, except that amplitude become slowly varying factor of z. Nonlinear source term is defined as

$$P_{sfg}(z,t) = P_{sfg}(z)e^{-i\omega_{sfg}t} + c.c. , \tag{2.1.5}$$

where $P_{sfg} = 4\varepsilon_0 d_{eff} E_s E_p$ and $E_i = A_i e^{ik_i z}$ ($i= s, p$). On substituting equation (2.1.4) and (2.1.5) in (2.1.3) and simplifying we get,

$$\frac{d^2 A_{sfg}}{dz^2} + 2ik_{sfg}\frac{dA_{sfg}}{dz} = \frac{-4d_{eff}\omega_{sfg}^2}{c^2} A_s A_p e^{i(k_s+k_p-k_{sfg})z} . \tag{2.1.5}$$

In accordance with slowly varying amplitude approximation, first term on left hand side can be neglected as it is too small and on simplification we get,

$$\frac{dA_{sfg}}{dz} = \frac{2id_{eff}\omega_{sfg}^2}{k_{sfg}c^2} A_s A_p e^{i\Delta kz} , \tag{2.1.6}$$

where $\Delta k = k_s + k_p - k_{sfg}$ is the wavevector mismatch. Equation (2.1.6) shows the variation in amplitude for SFG signal as a consequence of its coupling to signal and pump. Assuming signal and pump to be constant (undepleted) and integrating equation (2.1.6) from 0 to length L of the medium, we obtain

$$A_{sfg}(L) = \frac{2id_{eff}\omega_{sfg}^2 A_s A_p}{k_{sfg}c^2}\left(\frac{e^{i\Delta kL}-1}{i\Delta k}\right). \tag{2.1.7}$$

Intensity is defined as $I_i = 2n_i\varepsilon_0 c|A_i|^2$, $i = s, p$, or "sfg", $\omega_{sfg} = \frac{2\pi c}{\lambda_{sfg}}$. Thus the intensity of SFG upon simplification is given by

$$I_{\text{sfg}} = \frac{8\pi^2 d_{\text{eff}}^2 I_s I_p}{n_{\text{sfg}} n_s n_p \varepsilon_0 c \lambda_{\text{sfg}}^2} L^2 \operatorname{sinc}^2\left(\frac{\Delta k L}{2}\right). \tag{2.1.8}$$

Up-conversion requires non-zero overlap among spatial modes of the three involved fields. Overlap integral is given by

$$\Phi_{mnp} = \frac{\left|\int \Psi_{Sm}(\vec{\rho})\Psi_{Pn}(\vec{\rho})\Psi_{\text{SFG}p}^*(\vec{\rho}) d^2\vec{\rho}\right|^2}{\int \left|\Psi_{Sm}(\vec{\rho})\right|^2 d^2\vec{\rho} \int \left|\Psi_{Pn}(\vec{\rho})\right|^2 d^2\vec{\rho} \int \left|\Psi_{\text{SFG}p}^*(\vec{\rho})\right|^2 d^2\vec{\rho}} , \tag{2.1.9}$$

where *Sm*, *Pn* and SFG*p* correspond to *m*th signal mode, *n*th pump mode and *p*th SFG mode, respectively. The process coupling these modes will be referred to as <*m*, *n*, *p*>. The effective area of the process is inverse of the overlap integral:

$$A_{\text{eff}} = \frac{1}{\Phi_{\text{SFG}}} . \tag{2.1.10}$$

Output SFG power for <*m*, *n*, *p*> is given by

$$P_{\text{SFG}p} = \eta L^2 \Phi_{mnp} P_{Sm} P_{Pn} \sin c^2\left(\frac{\Delta k L}{2}\right), \tag{2.1.11}$$

where $\eta = \dfrac{8\pi^2 d_{\text{eff}}^2}{n_S^{\text{eff}} n_P^{\text{eff}} n_{\text{SFG}}^{\text{eff}} c\varepsilon_0 \lambda_{\text{SFG}}^2}$.

Our experimental investigation is for the χ^2 waveguide [27]. Potassium titanyl phosphate (KTP) and lithium niobate (LiNbO$_3$) are the two popular crystals for making such waveguides. Lithium niobate has largest nonlinear coefficient and for this reason we use Lithium Niobate waveguide which is periodically polled.

2.2 Quasi-phase-matching (QPM)

The concept of quasi-phase-matching has been perfected through material engineering. For a given phase mismatch Δk, sum-frequency wave reaches maximum value at $z = \dfrac{\pi}{\Delta k}$. After this distance the newly generated sum-frequency field starts to add destructively to the field created during propagation from 0 to $\pi/_{\Delta k}$ and net sum-frequency field starts to decrease. In the technique of QPM, the sign of the effective susceptibility $\chi^{(2)}$ (and, as a consequence, sign of d_{eff}) is flipped by electric-field polling of the medium after every $\pi/_{\Delta k}$ distance. This allows the sum-frequency field to continuously build instead of oscillating as a function of z. The phase mismatch for QPM is

$$\Delta k = \frac{2\pi}{\lambda_{\text{SFG}}} n_{\text{SFG}p}^{\text{eff}} - \frac{2\pi}{\lambda_S} n_{Sm}^{\text{eff}} - \frac{2\pi}{\lambda_P} n_{Pn}^{\text{eff}} - \frac{2\pi}{\Lambda} \ , \tag{2.1.12}$$

where λ is the wavelength, n^{eff} is the effective index, and Λ is the polling period of the waveguide. By dividing equation (2.1.38) on both sides by 2π, we can re-write as

$$\Delta = \Delta'_{mnp} - \Delta_{\text{QPM}} \ , \tag{2.1.13}$$

where

$$\Delta_{\text{QPM}} = \frac{1}{\Lambda} ,$$

and

10

$$\Delta'_{mnp} = \frac{n_{\text{SFG}p}^{\text{eff}}}{\lambda_{\text{SFG}}} - \frac{n_{Sm}^{\text{eff}}}{\lambda_S} - \frac{n_{Pn}^{\text{eff}}}{\lambda_P}$$

is the mismatch between the mth signal mode and nth pump mode on one hand and the pth SFG mode on the other hand. In our case, signal wavelength is 1540 nm, pump wavelength is 1560 nm, and the resultant SFG is generated at 775 nm. Output intensity of SFG is

$$I_{\text{sfg}}\left(\Delta k\right) = I_{\text{sfg}}\left(0\right)\text{sinc}^2\left(\frac{\Delta k L}{2}\right) \quad , \tag{2.1.14}$$

where $I_{\text{sfg}}(0)$ is the SFG intensity for $\Delta k = 0$. Therefore, the maximum intensity at the output takes place for $L = \dfrac{\pi}{\Delta k} = \dfrac{\pi}{2|\Delta|}$. Length of the waveguide and poling period is chosen in such a way that phase mismatch for the desired mode combination (m, n and p), satisfies $|\Delta| \leq \dfrac{\pi}{2L}$, so that SFG intensity is not reduced by the presence of phase mismatch.

2.3 Third-order nonlinear interactions in a few-mode fiber (FMF)

Many research efforts are currently being pursued increase the transmission capacity beyond the Shannon's limit of single fiber by using space-division multiplexing over multimode fiber or few-mode fiber (FMF). The FMF has the core area larger than SMF to transmit parallel data streams in a few independent spatial modes. Ideally, capacity of FMF is multiplied by the number of modes it

can support. Several types of FMF are available commercially, e.g., two-mode graded-index FMF, four-mode graded-index FMF, two-mode step-index FMF, and four-mode step-index FMF from OFS. We consider four-mode graded-index FMF, whose optical properties at 1550 m are listed in Table 2.1. below.

Table 2-1 Optical properties of four-mode graded-index FMF (OFS) at 1550 nm

Mode Field Diameter	$\mathrm{LP}_{01} = 10.7 \mu m$
	$\mathrm{LP}_{02} = 10.3 \mu m$
	$\mathrm{LP}_{11} = 10.8 \mu m$
	$\mathrm{LP}_{21} = 11.0 \mu m$
Effective Area	$\mathrm{LP}_{01} = 90 \mu m^2$
	$\mathrm{LP}_{02} = 184 \mu m^2$
	$\mathrm{LP}_{11} = 122 \mu m^2$
	$\mathrm{LP}_{21} = 166 \mu m^2$

The nonlinear effects originating from intensity dependence of refractive index of an optical fiber lead to phase that is a function of optical intensity. The intensity dependence of refractive index results in self-phase modulation (SPM), cross-phase modulation (XPM) and four-wave mixing (FWM). The wave equation, valid for all frequency components in a nonlinear medium is defined by

$$\nabla^2 \vec{E}_n - \frac{\varepsilon^{(1)}(\omega_n)}{c^2} \frac{\partial^2 \vec{E}_n}{\partial t^2} = \frac{1}{\varepsilon_0 c^2} \frac{\partial^2 \vec{P}_n^{\mathrm{NL}}}{\partial t^2} \ , \qquad (2.2.1)$$

where n=1,2,3……, $\vec{P}_n^{\mathrm{NL}} = \sum_j P_j e^{-i\omega_j t}$ is the nonlinear polarization,

$\vec{E}_n = \sum_j E_j e^{-i\omega_j t}$ is the field, c is speed of light in free space, ε_0 is the free space

permittivity and $\varepsilon^{(1)}(\omega_n) = n^2$ is the relative permittivity of the medium. Expanding and simplifying equation (2.2.1) will result in

$$\sum_j \left(\nabla^2 E_j + \frac{n_j^2 \omega_j^2}{c^2} E_j + \mu_0 \omega_j^2 P_j \right) e^{-i\omega_j t} = 0 \ . \tag{2.2.2}$$

So the wave equation in $\chi^{(3)}$ medium can be written as

$$\nabla^2 E_j + \frac{n_j^2 \omega_j^2}{c^2} E_j + \mu_0 \omega_j^2 P_j = 0, \tag{2.2.3}$$

where $E_j = A_j(z) F_j(x, y) e^{i\beta_j z}$ is the applied field with A_j being slowly varying amplitude, normalized so that the power $W_j = |A_j|^2$, $F_j(x, y)$ is the mode shape function such that $\int |F_j|^2 dx dy = \frac{1}{2\varepsilon_0 n_j c}$, and β_j is the propagation constant. Let us consider the case where electric field consists of four frequency components,

$$E_n(z,t) = E_B e^{-i\omega_B t} + E_I e^{-i\omega_I t} + E_{P1} e^{-i\omega_{P1} t} E_{P2} e^{-i\omega_{P2} t} \ .$$

First, consider the case of linear propagation [$P^{(3)} = 0$], which implies that amplitude $A_j(z)$ is constant. Equation (2.2.1) therefore can be written as

$\nabla^2 \vec{E}_n - \frac{\varepsilon^{(1)}(\omega_n)}{c^2} \frac{\partial^2 \vec{E_n}}{\partial t^2} = 0$. On expanding and simplifying we get

$$\nabla_{xy}^2 F_j(x, y) + \left[\left(\frac{n_j \omega_j}{c} \right)^2 - \beta_j^2 \right] F_j(x, y) = 0. \tag{2.2.4}$$

13

Now, let us consider the case with nonlinear polarization $[P^{(3)} \neq 0]$ which implies that amplitude $A_j(z)$ is not constant. Third-order nonlinear polarization [32] is given by

$$P^{(3)} = \varepsilon_0 \left(A + \frac{B}{2} \right) \left[\left(|E_B|^2 + 2|E_I|^2 + 2|E_{P1}|^2 + 2|E_{P2}|^2 \right) + 2E_1 E_2 \left(E_I \right)^* \right], \quad (2.2.4)$$

where $A = 6\chi^{(3)}_{1122}$, $B = 6\chi^{(3)}_{1221}$, and ε_0 is permittivity of free space. Consider (2.2.3), where applied field is $E_j = A_j(z)F_j(x,y)e^{i\beta_j z}$, which yields

$$A_j e^{i\beta_j z} \nabla^2_{x,y} F_j + \frac{\partial^2}{\partial z^2}\left(A_j(z)e^{i\beta_j z} \right) F_j + \left(\frac{n_j \omega_j}{c} \right) A_j F_j e^{i\beta_j z} = -\mu_0 \omega_j P_j^{(3)}, \quad (2.2.5)$$

where $j = B, I, P1$ or $P2$. We have

$$\frac{\partial^2}{\partial z^2}\left[A_j(z)e^{i\beta_j z} \right] = \left(\frac{\partial^2 A_j}{\partial z^2} + 2i\beta_j \frac{\partial A_j}{\partial z} - \beta_j A_j \right) e^{i\beta_j z}. \quad (2.2.6)$$

From the slow-varying envelop approximation we have $\frac{\partial^2 A}{\partial z^2} \approx 0$, and by using it in equation (2.2.6) we get

$$e^{i\beta_j z}\left\{ 2i\beta_j F_j \frac{\partial A_j}{\partial z} + A_j \left[\nabla^2_{xy} F_j + \left(\frac{n_j \omega_j}{c} \right)^2 F_j - \beta_j F_j \right] \right\} = -\mu_0 \omega_j^2 P_j^{(3)}. \quad (2.2.7)$$

From the linear polarization case [Equation (2.2.4)] we know that the term in the square brackets is zero, which leads us to

$$F_j \frac{\partial A_j}{\partial z} = -\frac{\mu_0 \omega_j^2 P_j^{(3)} e^{-i\beta_j z}}{2i\beta_j}. \quad (2.2.8)$$

14

Projection of Equation (2.2.8) onto the mode of the signal yields

$$\int dxdy F_j^* F_j \frac{\partial A_j}{\partial z} = -\frac{\mu_0 \omega_j^2 e^{-i\beta_j z}}{2i\beta_j} \int dxdy F_j^* P_j^{(3)} \quad . \tag{2.2.9}$$

Substitution of (2.2.4) into (2.2.9) will lead to

$$\frac{1}{2\varepsilon_0 n_j c} \frac{\partial A_j}{\partial z} = \frac{i\omega_j}{2n_j c}\left(A + \frac{B}{2}\right)\left\{ \int F_j^*\left(\left|A_j\right|^2 \left|F_j\right|^2 + 2\sum_{k\neq j}\left|A_k\right|^2 \left|F_k\right|^2\right)A_j F_j dxdy + \right. $$
$$\left. + \int F_j^* 2A_k A_l A_m^* F_k F_l F_m^* e^{i(\beta_k + \beta_l - \beta_m)z} dxdy \right\} e^{-i\beta_j z} \tag{2.2.10}$$

where indices j, k, l and m run over B, I, $P1$ and $P2$, and $\omega_j = \omega_k + \omega_l - \omega_m$.

Considering wavevector mismatch $\Delta\beta = \beta_1 + \beta_2 - \beta_I - \beta_B$ and by dividing the

equation (2.2.10) by $2\varepsilon_0 n_j c \int \left|F_j\right|^2 dxdy$ we get

$$\frac{\partial A_j}{\partial z} = \frac{i\omega_j}{4\varepsilon_0 n_j^2 c^2}\left(A + \frac{B}{2}\right)[(D_{SPM}\omega_j + 2\sum_{k\neq j} D_{XPM}\omega_k)A_j + 2A_1 A_2 A_i^* e^{i\Delta\beta z} D_{FWM}], \tag{2.2.11}$$

where

$$D_{SPM} = \frac{\int \left|F_j\right|^4 dxdy}{\left(\int \left|F_j\right|^2 dxdy\right)^2} \quad , \tag{2.2.12}$$

$$D_{XPM} = \frac{\int \left|F_j\right|^2 \left|F_k\right|^2 dxdy}{\left(\int \left|F_j\right|^2 dxdy \int \left|F_k\right|^2 dxdy\right)} \quad , \tag{2.2.13}$$

$$D_{FWM} = \frac{\int F_{P1} F_{P2} F_i^* F_B^* dxdy}{\left(\int \left|F_j\right|^2 dxdy\right)^2} \tag{2.2.14}$$

15

are the overlap integrals for self-phase modulation (SPM), cross-phase modulation (XPM), and four wave mixing (FWM). Effective areas for these processes are given by

$$A_{\text{SPM}}^{\text{eff}} = \frac{1}{D_{\text{SPM}}} \ , \qquad (2.2.15)$$

$$A_{\text{XPM}}^{\text{eff}} = \frac{1}{D_{\text{XPM}}} \ , \qquad (2.2.16)$$

$$A_{\text{FWM}}^{\text{eff}} = \frac{1}{D_{\text{FWM}}} \ , \qquad (2.2.17)$$

and effective area for one spatial mode is different from effective area for another mode. Simulation of SPM, XPM and FWM was done in MATLAB, and computed effective areas are listed in Table 2.2.

Table 2-2 Effective areas of SPM and XPM in FMF at 1550 nm

Self-phase modulation	$\text{Aeff}_{\text{LP01}} = 89\mu m^2$
	$\text{Aeff}_{\text{LP02}} = 189\mu m^2$
	$\text{Aeff}_{\text{LP11}} = 121\mu m^2$
	$\text{Aeff}_{\text{LP21}} = 168\mu m^2$
Cross-phase modulation	$\text{Aeff}_{\text{LP01LP11}} = 182\mu m^2$
	$\text{Aeff}_{\text{LP12LP02}} = 378\mu m^2$
	$\text{Aeff}_{\text{LP02LP21}} = 378\mu m^2$
	$\text{Aeff}_{\text{LP21LP01}} = 388\mu m^2$

2.4 Phase-matching condition

The nonlinear interactions among various spatial modes are determined by the phase-matching conditions, which were analyzed in detail in [28]. Here, we will provide derivations for the phase-matching conditions of reference [28]. For four-wave mixing to be present, energy conservation and phase-matching [29] have to be fulfilled. Energy conversation between three waves can be fulfilled in three ways in nonlinear medium. The optical angular frequency of the fourth wave ω_4 can assume one of the following three values.

$$\text{(PROCESS1)} \qquad \omega_4 = \omega_1 - \omega_2 + \omega_3 \quad , \tag{2.2.18}$$

$$\text{(PROCESS2)} \qquad \omega_4 = \omega_1 + \omega_2 - \omega_3 \quad , \tag{2.2.19}$$

$$\text{(PROCESS3)} \qquad \omega_4 = -\omega_1 + \omega_2 + \omega_3 \quad , \tag{2.2.20}$$

where ω_1, ω_2 and ω_3 are the optical angular frequency of the other three waves. For each of the three processes of (2.2.18)-(2.2.20) mentioned above, there is a corresponding phase matching condition

$$\text{(PROCESS1)} \qquad \beta^{(4)}(\omega_4) = \beta^{(1)}(\omega_1) - \beta^{(2)}(\omega_2) + \beta^{(3)}(\omega_3) \quad , \tag{2.2.21}$$

$$\text{(PROCESS2)} \qquad \beta^{(4)}(\omega_4) = \beta^{(1)}(\omega_1) + \beta^{(2)}(\omega_2) - \beta^{(3)}(\omega_3) \quad , \tag{2.2.22}$$

$$\text{(PROCESS3)} \qquad \beta^{(4)}(\omega_4) = -\beta^{(1)}(\omega_1) + \beta^{(2)}(\omega_2) + \beta^{(3)}(\omega_3) \quad , \tag{2.2.23}$$

where $\beta^{(i)}(\omega)$ with $i \in \{1, 2, 3, 4\}$, is the constant of propagation. By using Taylor series it can be expressed near an arbitrary angular optical frequency ω_0 as

$$\beta^{(i)}(\omega) = \beta_0{}^{(i)} - \beta_1{}^{(i)}(\Delta\omega) + \frac{\beta_2{}^{(i)}}{2}(\Delta\omega)^2 + \text{.......} \quad , \tag{2.2.24}$$

where $\quad \Delta\omega = \omega - \omega_0, \ \beta_n^{(i)} = d^n \beta^{(i)}(\omega) / d\omega^n, \quad$ and $\quad \beta_n^{(i)} = \beta_n{}^{(i)}(\omega)|_{\omega=\omega_0} \quad$ with $n \in \{0, 1, 2, ... \}$. From here on, we will consider only up to second-order terms, since higher-order dispersion terms are negligible and we can ignore them.

Table 2-3 Mapping of waves (*P1*, *P2*, *B*, *I*) and spatial modes (LP01, LP11)

Waves of (2.17)–(2.19)	ω_1	ω_2	ω_3	ω_4
Waves, name and mode	$\omega_{P1,11}$	$\omega_{B,01}$	$\omega_{P2,01}$	$\omega_{I,11}$

As shown in the Table 2.3, waves of (2.2.18)–(2.2.20) are assigned to different types of waves, pump, probe and idler and spatial modes LP01 or LP11. The angular frequency $\omega_{\text{wave,mode}}$ has two subscripts: "wave"-type takes the values *P1*, *P2*, *B*, and *I*, which corresponds to pump 1, pump 2, probe, and idler, respectively, and "mode" corresponds to LP01 and LP11 modes, respectively.

Let us consider PROCESS1 $(\omega_4 = \omega_1 - \omega_2 + \omega_3)$ and the corresponding phase matching condition $\beta^{(4)}(\omega_4) = \beta^{(1)}(\omega_1) - \beta^{(2)}(\omega_2) + \beta^{(3)}(\omega_3)$. Expanding phase-matching condition in accordance to equation (2.2.24) will yield

$$
\begin{aligned}
\beta_{0,11} + \beta_{1,11}\Delta\omega_{I,11} + \frac{\beta_{2,11}}{2}\Delta\omega_{I,11}^2 &= \beta_{0,11} + \beta_{1,11}\Delta\omega_{P1,11} + \frac{\beta_{2,11}}{2}\Delta\omega_{P1,11}^2 \\
&+ \beta_{0,01} - \beta_{1,01}\Delta\omega_{B,01} - \frac{\beta_{2,01}}{2}\Delta\omega_{B,01}^2 \quad (2.2.25) \\
&+ \beta_{0,01} + \beta_{1,01}\Delta\omega_{P2,01} + \frac{\beta_{2,01}}{2}\Delta\omega_{P2,01}^2.
\end{aligned}
$$

Rearranging equation (2.2.25) will give

$$
\begin{aligned}
\beta_{1,11}(\Delta\omega_{I,11} - \Delta\omega_{P1,11}) &+ \frac{\beta_{2,11}}{2}(\Delta\omega_{I,11}^2 - \Delta\omega_{P1,11}^2) \\
&= \beta_{1,01}(\Delta\omega_{P2,01} - \Delta\omega_{B,01}) + \frac{\beta_{2,11}}{2}(\Delta\omega_{P2,01}^2 - \Delta\omega_{B,01}^2),
\end{aligned}
$$

which after further simplification will give

$$(\Delta\omega_{I,11} - \Delta\omega_{P1,11}) \times \left[\beta_{1,11} + \frac{\beta_{2,11}}{2}(\Delta\omega_{I,11} + \Delta\omega_{P1,11}) \right]$$
$$= (\Delta\omega_{P2,01} - \Delta\omega_{B,01}) \times \left[\beta_{1,01} \frac{\beta_{2,11}}{2}(\Delta\omega_{P2,01} + \Delta\omega_{B,01}) \right] \qquad (2.2.26)$$

We know that $\Delta\omega = \omega - \omega_0$, which reduces equation (2.2.26) to

$$(\omega_{I,11} - \omega_{P1,11}) \left[\beta_{1,11} + \frac{\beta_{2,11}}{2}(\Delta\omega_{I,11} + \Delta\omega_{P1,11}) \right]$$
$$= (\omega_{P2,01} - \omega_{B,01}) \left[\beta_{1,01} + \frac{\beta_{2,11}}{2}(\Delta\omega_{P2,01} + \Delta\omega_{B,01}) \right] . \qquad (2.2.27)$$

We know from PROCESS1 that $\omega_4 - \omega_1 = \omega_3 - \omega_2$. Therefore, equation (2.2.27) reduces to

$$\beta_{1,11} + \frac{\beta_{2,11}}{2}(\Delta\omega_{I,11} + \Delta\omega_{P1,11}) = \beta_{1,01} + \frac{\beta_{2,11}}{2}(\Delta\omega_{P2,01} + \Delta\omega_{B,01}) . \quad (2.2.28)$$

The phase-matching for FWM PROCESS1 of (2.2.21) and PROCESS2 of (2.2.22) leads to identical conditions (2.2.28). $\beta_{n,\mathrm{mode}}$ is the nth order dispersion term for each mode and $\Delta\omega_{\mathrm{wave,mode}} = \omega_{\mathrm{wave,mode}} - \omega_0$ are relative angular frequencies. For each spatial mode, the inverse group velocity (IVG) at frequency ω is given by $\beta_1(\omega) = \beta_1 + \beta_2(\omega - \omega_0)$. Equation (2.2.28) can be interpreted as follows: when group velocities evaluated at the average frequencies of the two waves present in each spatial mode are equal, the phase matching for intermodal FWM is achieved. Equation (2.2.28) is also independent of β_0 of each spatial

20

mode and thus even in the presence of fluctuations of β_0 [30] common to each spatial mode [31] the phase-matching remains fulfilled.

Let us now derive the phase-matching condition for the FWM PROCESS3 of (2.2.23). Consider $\omega_4 = -\omega_1 + \omega_2 + \omega_3$ and the corresponding phase-matching condition $\beta^{(4)}(\omega_4) = -\beta^{(1)}(\omega_1) + \beta^{(2)}(\omega_2) + \beta^{(3)}(\omega_3)$. Expanding phase-matching condition in accordance to equation (2.22) will give

$$
\begin{aligned}
\beta_{0,11} + \beta_{1,11}\Delta\omega_{I,11} + \frac{\beta_{2,11}}{2}\Delta\omega^2_{I,11} &= -\beta_{0,11} - \beta_{1,11}\Delta\omega_{P1,11} - \frac{\beta_{2,11}}{2}\Delta\omega^2_{P1,11} \\
&\quad + \beta_{0,01} + \beta_{1,01}\Delta\omega_{B,01} + \frac{\beta_{2,01}}{2}\Delta\omega^2_{B,01} \qquad (2.2.29) \\
&\quad + \beta_{0,01} + \beta_{1,01}\Delta\omega_{P2,01} + \frac{\beta_{2,01}}{2}\Delta\omega^2_{P2,01} \; .
\end{aligned}
$$

Rearranging and simplifying equation (2.2.29) will give

$$
\begin{aligned}
\beta_{1,01}(\Delta\omega_{P2,01} + \Delta\omega_{B,01}) &= \frac{\beta_{2,11}}{2}(\Delta\omega^2_{P1,11} + \Delta\omega^2_{I,11}) - \frac{\beta_{2,01}}{2}(\Delta\omega^2_{P2,01} + \Delta\omega^2_{B,01}) \\
&\quad + 2(\beta_{0,11} - \beta_{0,01}) + \beta_{1,11}(\Delta\omega_{P1,11} + \Delta\omega_{I,11}) \; .
\end{aligned} \qquad (2.2.30)
$$

Using $\Delta\omega_{P2,01} + \Delta\omega_{B,01} = \omega_{P2,01} + \omega_{B,01} - 2\omega_0$, $\Delta\omega_{I,11} + \Delta\omega_{P1,11} = \omega_{I,11} + \omega_{P1,11} - 2\omega_0$, and energy conservation $\omega_{I,11} + \omega_{P1,11} = \omega_{B,01} + \omega_{P2,01}$, we obtain from equations (2.31), (2.32) and (2.33):

$$
\begin{aligned}
\frac{\beta_{2,11}}{2}(\Delta\omega^2_{P1,11} + \Delta\omega^2_{I,11}) - \frac{\beta_{2,01}}{2}(\Delta\omega^2_{P2,01} + \Delta\omega^2_{B,01}) + \\
+ (\beta_{1,11} - \beta_{1,01})(\Delta\omega_{P1,11} + \Delta\omega_{I,11}) + 2(\beta_{0,11} - \beta_{0,01}) = 0 \; .
\end{aligned} \qquad (2.2.31)
$$

21

From Equation (2.2.31) it is clear that phase-matching depends on $\beta_{0,11} - \beta_{0,01}$ and therefore is highly sensitive to fluctuations with distance of the relative β_0 between modes.

We have described mode interactions in a few mode fiber and derived some important relations for mode overlap integrals and phase-matching conditions. Even though the phase-matching condition has been derived for two-mode interaction, we expect similar pairwise mode interactions to happen in the four-mode fiber.

Chapter 3

Experiments

We start this chapter by discussion the oven and temperature controller we have built for the PPLN waveguide and then proceed with the description of the experimental setup for spatial-mode-selective frequency up-conversion.

3.1 Oven

Oven is made using aluminum metal as it has very good thermal conductivity. Dimensions of oven are 50 mm×25 mm×25 mm in length, width and height, respectively. A grove is made on top of oven to place waveguide and it is of dimensions 50 mm×6.5 mm×1 mm in length, width and height, respectively. Lightest grit sand paper was used to rid of scratches and get a smooth surface. Arctic silver thermal compound was applied on grove before placing waveguide, which helps improving thermal conductivity and keeps the waveguide from sliding along the grove. Six holes were drilled along the sides away from the grove, which helps in screwing the oven to the Thorlabs 3D translation stage using Teflon screws. A hole of diameter 9.6 mm is made all along the length of the oven to place the heater. The diameter of the hole was smaller than actual requirement and then a reamer was used to scrape around hole for exact fit of the heater in hole so that no air gap is left between heater and module. A heat conducting gel was applied around the heater before inserting it in hole. Two Teflon sheets of dimensions 50 mm×25 mm×3.175 mm were used to isolate

23

oven from the stage and these sheets along with Teflon screws help in preventing heat transfer to the stage. A resistance temperature detector (RTD) is used to sense temperature and is screwed on surface of the oven close to the waveguide. An aluminum plate of dimensions 50 mm×25 mm×4 mm is placed on top surface and is screwed to the top of the oven.
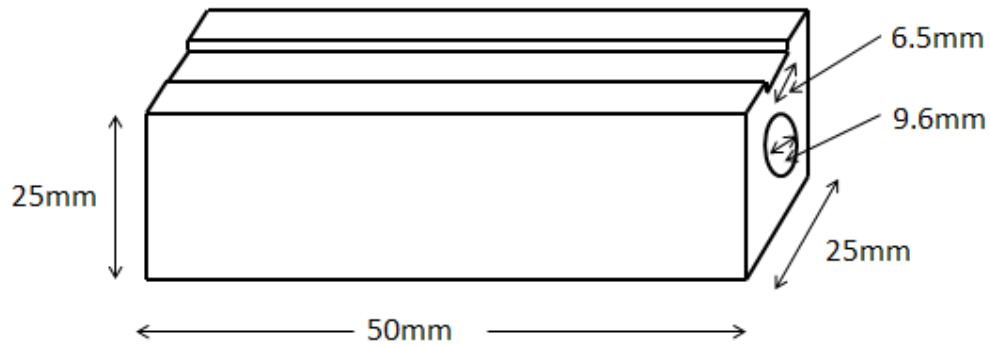

Figure 3-1 Schematic of oven with dimensions.

3.2 Temperature controller

A temperature controller is used to regulate the temperature in oven. Resistance temperature detector (RTD) mounted on the oven's surface will sense the temperature of the oven and based on the pre-set temperature in controller, a decision will be taken by controller either to turn on or turn off the heater, which is connected through a solid-state relay. Circuit diagram is shown below,
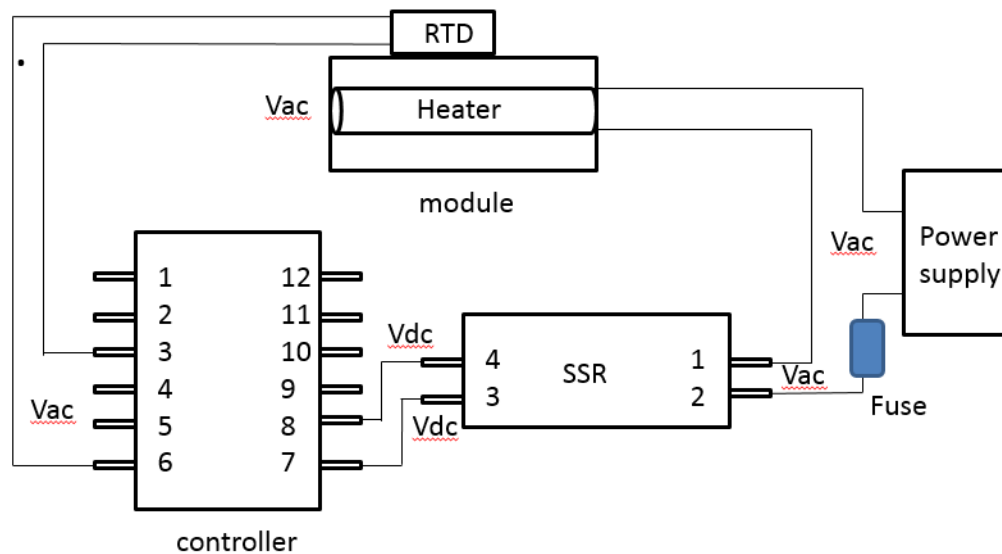
Figure 3-2 Circuit of temperature controller.

The proportional-integral-derivative (PID) control is a control loop feedback mechanism which continuously monitors the difference between process variable and SET value. PID uses three important control variables, proportional response, integral response and derivative response.

Proportional response (Pn) gives the output depending upon the error value which is the difference between the actual temperature and SET temperature. The error value is multiplied by the proportional constant to get output. Output is zero when the error value is zero. If the Pn is too low then it will result in oscillations and if it's too high it will take too much time to complete loop. In our case we have used 10. It is evident that the error value will never become zero and there

always exists a steady-state error. Integral response (In) will integrate this error over a period of time and takes necessary action to remove that error. It limits the speed of response and affects the system stability. In our case, we have set In to 25. Derivative response (Dn) anticipates the future behavior of error and output depends on rate of change of error times the derivative constant. In our case we set Dn to 25. The integral deviation offset correction (ioFn) improves the speed in which the process value reaches the set point. Very high value will result in oscillations. We have set it to 4 in our setup.

3.3 Experimental setup for spatial-mode-selective frequency up-conversion

Tunable laser sources are set at wavelength 1540 nm (signal) and 1560 nm (pump), multiplexed using wavelength-division multiplexer, and pre-amplified using EDFA amplifier. Multiplexed beams are then modulated using a high extinction ratio Mach-Zehnder modulator (MZM). The light is then passed through second EDFA amplifier for high-power amplification. Multiplexed beams of 1540 nm and 1560 nm are then separated, modulated by Spatial Light Modulator (SLM), then recombined and transmitted through PPLN waveguide. The light is then passed through long-pass filter which reflects up-converted signal to be focused onto a CCD camera, whereas infrared light passes through the long-pass filter and is focused onto IR camera. Experiment set up is shown in the Figure 3-3
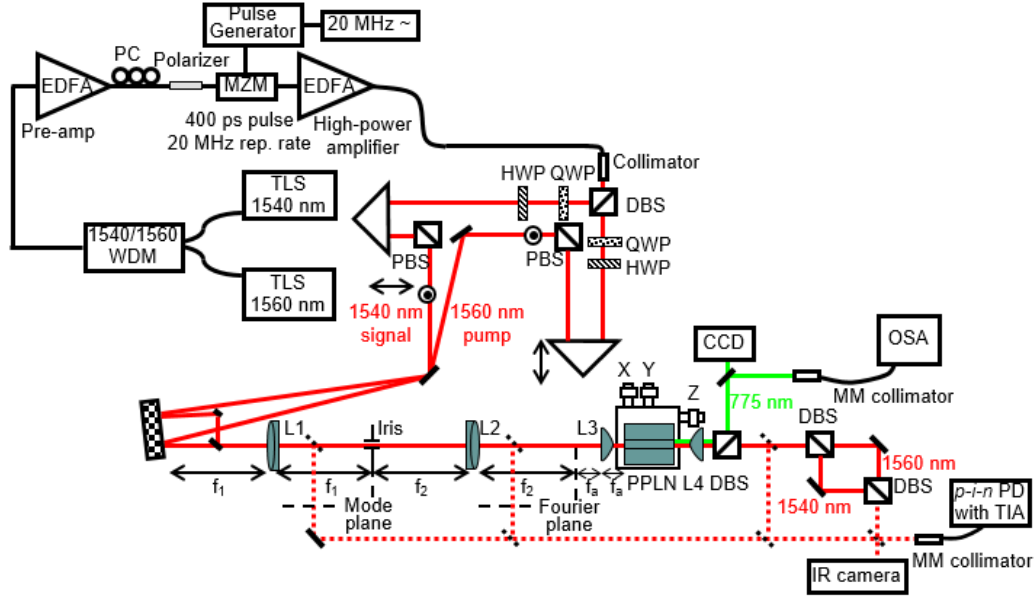
Figure 3-3 Experimental setup.

Wavelength-division multiplexer (WDM) is used to combine two single-mode signals from two tunable laser sources, of which one is pump of wavelength 1560 nm and other is signal of wavelength 1540 nm. Wavelength-division multiplexer is used because of its very small insertion loss. This combined signal is amplified using an Erbium-Doped Fiber Amplifier (EDFA) from Highwave Optical Technologies, which has a gain of 23 dB. Multiplexed light is then passed through in-line polarizer to become vertically polarized. Polarization-maintaining fiber is used to transmit light from polarizer to modulator. This vertically-polarized light is modulated by an ultra-high extinction ratio Mach-Zehnder Modulator (MZM), which is an electro-optic modulator. RF signal and bias voltage to MZM is supplied from external modules. Optical pulses generated have a period of 50 ns

with pulse width of 400 ps. By using a different delay in external NuCrypt RF generator driven by a 20-MHz clock it is possible to generate optical pulses of a different width. Appropriate bias voltage is supplied by controlling both course and fine knobs in the external voltage supply to get high extinction ratio for the optical pulse in MZM. These pulses are again amplified using the high-power EDFA from Keopsys that has a gain of 30 dB.

Fiber collimator is used to transfer amplified pulsed light from optical fiber to free space. The fiber end is firmly fixed at the focal distance of collimator lens so that the output is perfectly collimated. $1/e$ intensity beam radius of the light from collimator is 1.02 mm. Dichroic beam splitter (DBS) from Chroma Technology is used to de-multiplex signal of 1540 nm and pump of 1560 nm. DBS was custom made for this experiment purpose and has 50% transmission and 50% reflection at 1554.5 nm for 45 degree incidence. The model number of this DBS is T1552Ipxxr, its size is $21 \times 26 \times 6$ mm and in our experiment it reflects 1540 nm light pulses at an efficiency of 94.5% and 1560 nm light pulses is transmitted at efficiency 96.0% when light is incident at 45°. The separated pump and signal go through separate pairs of quarter-wave plate (QWP) and half-wave plate (HWP), which convert their polarizations to vertical. Then a right-angled prisms are used in both legs to reflect the beam by 180°. They are mounted on single-axis translation stages with standard micrometers. These stage in both legs help us in making sure that path lengths travelled by both the pump and the signal are the

28

same. Then each beam passes through a pair of polarization beam splitters that reflects only vertical polarization, which is important for us because spatial light modulator works only with vertical polarization component. By using a set of mirrors we direct both pump light pulses of 1560 nm and signal light pulses of 1540 nm on to the SLM at different locations for modulation.

Spatial light modulator (SLM) from Meadowlark Optics (formerly known as Boulder Nonlinear Systems) is an electrically programmable device that phase-modulates reflected light according to the image loaded into it. XY phase series SLMs used in our experiment converts incident light into the desired spatial shape according to the digitized data loaded in to it, preserving the coherence. This feature makes SLMs appropriate for a variety of applications including optical tweezers, beam steering, pulse shaping, diffractive optics and more. Cross-section illustration of liquid crystal SLM is shown below.
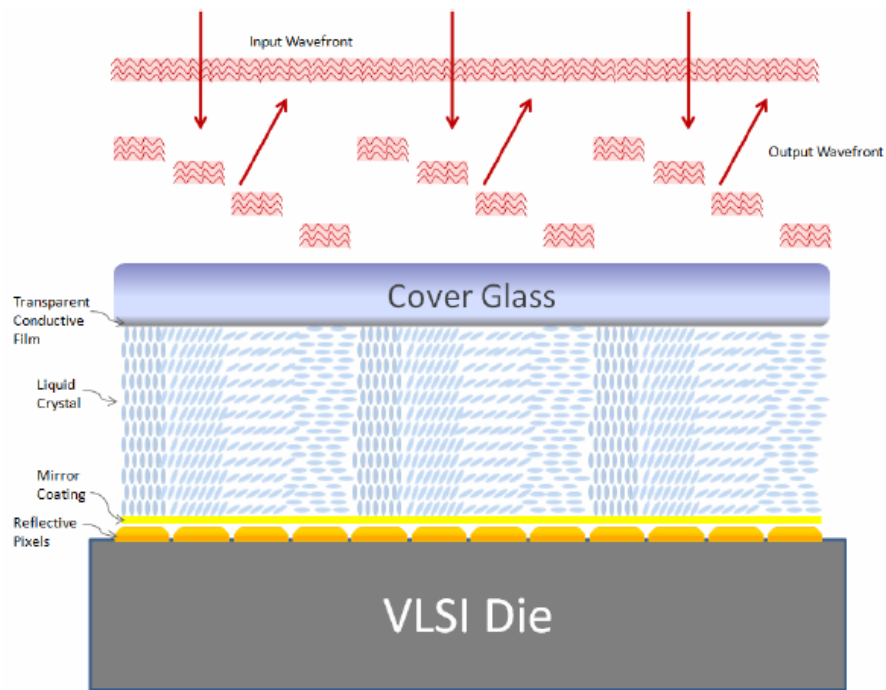
Figure 3-4 Cross-section view of SLM (picture taken from manual [33]).

As shown in the Figure 3-4 vertically-polarized light enters from the top, passes through cover glass, transparent conductive film, and liquid crystal layer, and is reflected by the shiny pixels electrodes back in the same path. Each pixel will receive a drive signal from driver board and this analog voltage on each pixel will produce electric field between pixel and cover glass. This electric field will in turn produce changes in the optical parameters in the LC layer. Each pixel can be controlled independently, by loading different voltages to each pixel different phase pattern can be obtained.

The XY phase series of SLM is made of nematic liquid crystal which have variable electro-optic response to voltage. These molecules are parallel to cover

glass and backplane when no voltage is applied and incident light experiences the largest index difference between extraordinary and ordinary axis. Molecules are nearly perpendicular when maximum voltage is applied, with index difference between extraordinary and ordinary axis is close to zero. If linearly polarized light parallel to extraordinary axis is incident, then a pure voltage-dependent phase shift will be observed. If the pixel is programed for maximum voltage, a minimum phase delay is applied and if no voltage is applied, maximum phase retardation will be applied. Each of the SLM pixels is independently programmable to 65,535 discrete voltage levels, all providing phase modulation. The applied phase modulation consists of a fast-spatially-varying component (checkerboard pattern among pixels) and a slow-varying component. The fast-varying phase modulation is subsequently converted into the amplitude modulation by an iris put in the Fourier plane of a 4*f* lens system, which rejects high spatial-frequency components, so that the amplitude of the remaining zero-order component is determined by the slow-varying contrast of the checkerboard pattern on the SLM.

Both pump and signal after getting modulated on SLM are combined using right-angle prism and dichroic beam combiner, and the combined beam is coupled into the PPLN waveguide through a telescopic (4*f*) arrangement of lenses with focal lengths 250 mm and 200 mm and an aspheric lens of focal length 6.25 mm. PPLN waveguide is placed on a oven maintained at phase-matching temperature

31

of 82.3°C. Oven is placed on a Thorlabs 3-axis NanoMax translation stage with differential adjusters. After the first lens in telescopic arrangement, at the focal plane of the lens we use an iris to block the higher-order very diffraction spots from the SLM, and only the bright zero-order-diffraction beam passed. Aspheric lens is used as the final lens to couple spatial modes into PPLN waveguide. These aspheric lens help us to eliminate spherical aberrations, providing diffraction-limited beam at the PPLN waveguide facet. The beam profiles imposed by the SLM correspond to Fourier transform of the beam profiles on the waveguide facet.

Output from the waveguide is passed through microscope objective and then a long-pass filter is used to separate the up-converted signal from the original infrared signal and the pump. Reflected up-converted signal is imaged onto a Panasonic visible light camera, whereas in the transmitted beam the pump is removed by passing through several DBS, and only 1540 nm signal is incident upon Xenics infrared camera.

Chapter 4

Results

Signal at wavelength 1540 nm and pump at wavelength 1560 nm are coupled into multimode PPLN waveguide for mode-selective frequency up-conversion. We have two desired cases, shown in Table 4.1 below.

Table 4-1 Desired mode combination process

Signal at 1540 nm	Pump at 1560 nm	Up-converted signal at 775 nm
HG01	HG00	HG01
HG00	HG01	HG01

Signal at wavelength 1540 nm from ANDO tunable laser is set to 2 dBm power and pump at wavelength 1560 nm from Yenista (formerly Photonetics) laser is at 4 dBm. Input powers to PPLN waveguide measured before aspheric lens is shown in Table 4.2 below.

Table 4-2 Signal and pump powers before coupling into PPLN

Modes	Signal average power	Pump average power	Signal peak power	Pump peak power
HG00	2.67 mW	13.77 mW	333.75 mW	1720 mW
HG01	2.06 mW	21.23 mW	257.5 mW	2650 mW

Output beam from PPLN waveguide is passed through long-pass filter, two dichroic beam splitters, and interference filter (IF). At long-pass filter, up-

converted signal is reflected and is incident on Panasonic camera. Transmitted infrared beam which contains signal and pump is passed through two dichroic mirrors and IF filter to separate 1540 nm and 1560 nm, and only signal 1540 nm is incident on Xenics infrared camera. The measured powers at Xenics and Panasonic camera locations are given in Table 4.3 below.

Table 4-3 Powers measured on cameras after PPLN

	Both beams case	Only 1540 nm beam	Only 1560 nm beam	Camera source
$HG00^{1540}+HG00^{1560}$	1052.78	1072.5	6.9	Xenics unit in a.u.
	58.33	0.30	1.23	Visible power meter in μW
$HG01^{1540}+HG00^{1560}$	181.08	1407.0	0.19	Xenics in a.u.
	1985.32	1.36	1.23	Visible power meter in μW
$HG00^{1540}+HG01^{1560}$	214.5	1096.1	0.22	Xenics in a.u.
	1395.62	0.30	1.89	Visible power meter in μW
$HG01^{1540}+HG01^{1560}$	1378.42	1379.28	6.85	Xenics in a.u.
	15.91	1.36	1.89	Visible power meter in μW

Images of the signal, pump, and up-converted signal captured in Xenics and Panasonic cameras are shown in Table 4.4 below.

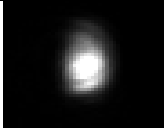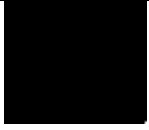Table 4-4 Signal, pump, and up-converted beam profiles captured on camera
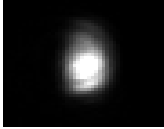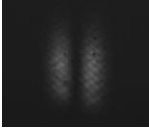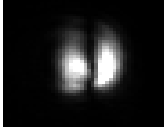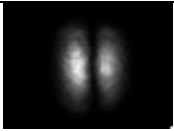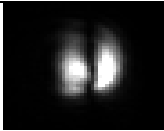
Signal (1540 nm)	Pump (1560 nm)	Up-converted (775 nm)

Table 4-5 Internal and external efficiencies of mode-selective frequency-up-

conversion

Signal^{1540} + Pump^{1560}	Photon Conversion Efficiency (Internal)	Photon Conversion Efficiency (External)
$HG_{00}^{1540} + HG_{00}^{1560}$	1.8%	1.1%
$HG_{01}^{1540} + HG_{00}^{1560}$	87%	48%
$HG_{00}^{1540} + HG_{01}^{1560}$	80%	26%
$HG_{01}^{1540} + HG_{01}^{1560}$	0.06%	0.4%

Table 4.5 gives the photon conversion efficiencies, and it is very clear that in our desired cases, signal mode HG00 and pump HG01 or signal mode HG01 and pump mode HG00, internal conversion efficiencies measured from the signal depletion are 80% and 87%, respectively. External efficiencies are 26% and 48%, respectively. External photon conversion efficiency is measured by dividing the sum-frequency power by twice the signal power before the aspheric lens and thus includes the coupling and propagation losses in the PPLN waveguide. Very low photon conversion has happened for both undesired cases, with the crosstalk below −16.4 dB.

Chapter 5

Conclusions

We have experimentally demonstrated the spatial-mode-selective frequency up-conversion of 1540 nm signal using 1560 nm pump by coupling in a two-mode Periodically Poled Lithium Niobate (PPLN) waveguide. Selective up-conversion of either zero-order or first-order mode is achieved by choosing the appropriate pump mode. Up-conversion efficiency of more than 80% and crosstalk of less than −16 dB have been demonstrated.

These results can be used for building spatial-mode de-multiplexers for classical and quantum communications.

Appendix

Product Details

Table A1 Product, model number, and specifications of components used in

optical setup for frequency-up-conversion

Company	Product	Model	Specifications/Description
JDS Uniphase	Tunable Laser Source	SWS16101	C Band
ANDO	Tunable Laser Source	AQ4321A	
	WDM		
	Polarizer		
Highwave Optical Technologies	EDFA Pre Amplifier		
EOSPACE	Modulator	Ultra-High extinction ratio modulator	
Chroma Technologies	Dichroic Beam Splitter	T1552Ipxxr	At 45 degree angle of incidence for 1554.5nm, 50% transmission and 50% reflection
Thorlabs	Quarter wave	WPQ05M-	½" mounted zero order QWP,

	plate	1550	transmission at design wavelength 1550nm is >98%
Thorlabs	Half wave plate	WPH05M-1550	½" mounted zero order HWP, transmission at design wavelength 1550nm is >98%
Thorlabs	Polarizing beam splitter	PBS25-1550	1" PBS at designed wavelength 1550nm, reflects S polarization and allows P polarization with polarization extinction ratio of 100:1
Thorlabs	Right-Angle prism mirror	MRA05-P01	180 degree reflection when light incident on hypothesis
Meadowlark Optics	Spatial light modulator		
Thorlabs	Achromatic Doublet	AC254-250/200-C-ML	Achromatic doublets designed for IR have focal length is 250mm/200mm with clear aperture 90% of lens diameter.
Thorlabs	Aspheric lens	A110TM-C	Focal length 6.24mm, NA=0.4
Thorlabs	Longpass	DMLP1180	50% transmission/ reflection at

	Dichroic Mirror		1180nm. Longer wavelengths are transmitted and shorter are reflected

Table A2 Product, model number, and cost of components used in controller

Product	Modal number	Cost
Cartridge heater	CSS-10150/120	$19
RTD	RTD-830	$71
Controller	CN7523	$110
Solid state relay	SSRL240DC10	$22
Fuse	KAX-10	$35
Fuse holder	FB-1	$30

References

[1] R.-J. Essiambre, G. Kramer, P. J. Winzer, G. J. Foschini, and B. Goebel, "Capacity limits of optical fiber networks," J. Lightw. Technol., vol. 28, no. 4, pp. 662–701, Feb. 2010.

[2] A. R. Chraplyvy, "The coming capacity crunch," presented at the presented at the 35th Eur. Conf. Opt. Commun., Vienna, Austria, 2009.

[3] Richardson, D. J., Fini, J. M. & Nelson., L. E. Space-division multiplexing in optical fibres.Nat. Photonics 7, 354–362 (2013).

[4] Choi, S.-K., Vasilyev, M., and Kumar, P., "Noiseless optical amplification of images," Phys. Rev. Lett. 83(10), 1938–1941 (1999); erratum: Phys. Rev. Lett. 84(6), 1361–1361 (2000).

[5] Lantz, E., and Devaux, F., "Parametric amplification of images: from time gating to noiseless amplification," IEEE J. Sel. Topics Quantum Electron. 14(3), 635–647 (2008).

[6] Annamalai, M., and Vasilyev, M., "Phase-sensitive multimode parametric amplification in a parabolic-index waveguide," IEEE Photon. Technol. Lett. 24(21), 1949–1952 (2012).

[7] Vasilyev, M., Annamalai, M., Stelmakh, N., and Kumar, P., "Quantum properties of a spatially-broadband traveling-wave phase-sensitive optical parametric amplifier," J. Mod. Opt. 57(19), 1908–1915 (2010).

[8] Annamalai, M., Stelmakh, N., Vasilyev, M., and Kumar, P., "Spatial modes of

phase-sensitive parametric image amplifiers with circular and elliptical Gaussian pumps," Opt. Express 19(27), 26710–26724 (2011).

[9] Annamalai, M., Stelmakh, N., Kumar, P., and Vasilyev, M., "Compact representation of the spatial modes of a phase-sensitive image amplifier," Opt. Express 21(23), 28134–28153 (2013).

[10] C. H. Bennett and G. Brassard. Quantum cryptography: Public key distribution and coin tossing. In Proceedings of IEEE International Conference on Computers, Systems and Signal Processing, 1984.

[11] R. J. Hughes, G. L. Morgan, and C. G. Peterson. Quantum key distribution over a 48-km optical ¯ber network. J. Modern Optics, 47:533, 2000.

[12] M. Bourennane, A. Karlsson, J. P. Ciscar, and M. Math¶es. Single-photon counters in the telecom wavelength region of 1550 nm for quantum information processing. J. Modern Optics, 48:1983{1995, 2001.

[13] D. Stucki et al. Photon counting for quantum key distribution with Peltier cooled InGaAs/InP APDs. Modern Optics, 48:1967{1981, 2001.

[14] Y. Liang and H. Zeng, "Single-photon detection and its applications," Sci. Chin. Phys. Mech. Astronomy, vol. 57, no. 7, pp. 1218–1232, 2014.

[15] Kuo, P. S., Pelc, J. S., Slattery, O., Kim, Y. S., Fejer, M. M., and Tang, X., "Reducing noise in single-photon-level frequency conversion," Opt. Lett. 38(8), 1310–1312 (2013).

[16] Albota, M. A., and Wong, F. N. C., "Efficient single photon counting at 1.55 μm

by means of frequency conversion," Opt. Lett. 29(13), 1449–1451 (2004).

[17] Thew, R. T., Zbinden, H., and Gisin, N., "Tunable upconversion photon detector," Appl. Phys. Lett. 93(7), 071104 (2008).

[18] Kumar, P., "Quantum frequency conversion," Opt. Lett. 15(24), 1476–1478 (1990).

[19] Huang, J., and Kumar, P., "Observation of quantum frequency conversion," Phys. Rev. Lett. 68(14), 2153–2156 (1992).

[20] Vasilyev, M., and Kumar, P., "Frequency up-conversion of quantum images," Opt. Express 20(6), 6644–6656 (2012).

[21] Roelofs, M. G., Suna, A., Bindloss, W., and Bierlein, J. D., "Characterization of optical waveguides in $KTiOPO_4$ by second harmonic spectroscopy," J. Appl. Phys. 76(9), 4999–5006 (1994).

[22] Delaubert, V., Lassen, M., Pulford, D. R. N., Bachor, H.-A., and Harb, C. C., "Spatial mode discrimination using second harmonic generation," Opt. Express 15(9), 5815–5826 (2007).

[23] Kurz, J. R., Huang, J., Xie, X. P., Saida, T., and Fejer, M. M., "Mode multiplexing in optical frequency mixers," Opt. Lett. 29(6), 551–553 (2004).

[24] Kurz, J. R., Xie, X. P., and Fejer, M. M., "Odd waveguide mode quasi-phase matching with angled and staggered gratings," Opt. Lett. 27(16), 1445–1447 (2002).

[25] Mosley, P. J., Christ, A., Eckstein, A., and Silberhorn, C., "Direct measurement

of the spatial-spectral structure of waveguided parametric down-conversion," Phys. Rev. Lett. 103(23), 233901 (2009).

[26] Karpinski, M., Radzewicz, C., and Banaszek, K., "Experimental characterization of three-wave mixing in a multimode nonlinear $KTiOPO_4$ waveguide," Appl. Phys. Lett. 94(18), 181105 (2009).

[27] Kwon, Y. B., and Vasilyev, M., "Mode-selective frequency up-conversion in a $\chi(2)$ waveguide," Proc. of SPIE 8964, 896421 (2014).

[28] R. Essiambre, M. A. Mestre, R. Ryf, A. H. Gnauck, R. W. Tkach, A. R. Chraplyvy, Y. Sun, X. Jiang, and R. Lingle, "Experimental investigation of inter-modal four-wave mixing in few-mode fibers," IEEE Photon. Technol. Lett., vol 25, no. 6, pp. 539–542, January 2013.

[29] R. H. Stolen, J. E. Bjorkholm, and A. Ashkin, "Phase-matched three- wave mixing in silica fiber optical waveguides," Appl. Phys. Lett.,vol. 24, no. 7, pp. 308–310, 1974.

[30] J. Cheng, et al., "Intermodal Čerenkov radiation in a higher-order-mode fiber," Opt. Lett., vol. 37, no. 21, pp. 4410–4412, Nov. 2012.

[31] R.-J. Essiambre, et al., "Demonstration of broadband inter-modal four-wave mixing in graded-index few-mode fibers," in Proc. OFC Conf., 2013, pp. 1–3, paper OM3B.2.

[32] R. W. Boyd, "Nonlinear Optics," 3rd ed, Academic Press, 2008.

[33] *Manual for XY-series SLMs*, Meadowlark Optics, 2014.

Biographical Information

Mohan Giribabu received Bachelor of Engineering in Electronics and Communication Engineering from Visvesvaraya Technological University-Belgaum, India. He is interested in nonlinear optics and communication systems. Mohan is Cricketer by passion and enjoys playing Badminton.